ChemPubSoc Europe

DOI: 10.1002/celc.201800729

CHEMELECTROCHEM Articles

Special Issue

Mean Intrinsic Activity of Single Mn Sites at $LaMnO_3$ Nanoparticles Towards the Oxygen Reduction Reaction

Veronica Celorrio,*[a, e] Laura Calvillo,[b] Celeste A. M. van den Bosch,[c] Gaetano Granozzi,[b] Ainara Aguadero,[c] Andrea E. Russell,[d] and David J. Fermín*[a]

$LaMnO_3$ has been identified as one of the most active systems towards the 4-electron oxygen reduction reaction (ORR) under alkaline conditions, although the rationale for its high activity in comparison to other perovskites remains to be fully understood. $LaMnO_3$ oxide nanoparticles are synthesised by an ionic-liquid based method over a temperature range of 600 to 950 °C. This work describes a systematic study of the $LaMnO_3$ properties, from bulk to the outermost surface layers, as a function of the synthesis temperature to relate them to the ORR activity. The bulk and surface composition of the particles are characterised by transmission electron microscopy, X-ray diffraction, X-ray absorption and X-ray photoemission spectroscopy (XPS), as well as low-energy ion scattering spectroscopy (LEIS). The particle size and surface composition are strongly affected by temperature, although the effect is non-monotonic. The number density of redox active Mn sites is obtained from electrochemical measurements, and correlates well with the trends observed by XPS and LEIS. ORR studies of carbon-supported $LaMnO_3$ employing rotating ring-disk electrodes show a step increase in the mean activity of individual surface Mn sites for particles synthesised above 700 °C. Our analysis emphasises the need to establish protocols for quantifying *turn-over frequency* of single active sites in these complex materials to elucidate appropriate structure-activity relationships.

1. Introduction

The development of efficient electrocatalysis for the oxygen reduction (ORR) and evolution reactions (OER) are key challenges in the field of electrochemical energy conversion, underpinning key technologies such as fuel cells, solar water splitting, CO_2 conversion and metal-air batteries.[1–2] Although noble metal–based catalysts are widely used as ORR electrocatalyst in fuel cells, the search for earth-abundant catalysts with high activity and stability has brought the attention to transition metal oxides.[3–5] Among this vast family of compounds, manganese based perovskites, in particular $LaMnO_3$, have been identified among the most active systems for the 4-electron ORR under alkaline conditions.[6–10] However, the rationale for the activity of these materials remains to be fully elucidated.

Shao-Horn and co-workers correlated the high activity of $LaMnO_3$ to the strong affinity to O_2 as a result of the single electron occupancy at the e_g orbitals.[11] Further, DFT studies have proposed that ORR is initiated by O_2 adsorption on-top of surface Mn sites.[12–15] However, several studies have shown that Mn orbital occupancy increases at potentials in which ORR is promoted, which is a unique characteristic of $LaMnO_3$, in comparison to other first row lanthanides.[7,16] In a recent study, Gobaille-Shaw and co-workers found that the turn-over rate for ORR has a second order dependence on the number of reducible Mn-sites at the surface.[17] The role of the Mn coordination has also been considered, with studies postulating that the rhombohedral structure is more active than the orthorhombic form,[11] while others reporting little contrast in the reactivity of the two phases.[18] The range of activities reported for $LaMnO_3$ is very large as reviewed by Stoerzinger et al.,[6] suggesting that synthesis protocols may play a crucial role in determining the activity of this oxide.

In this work, we systematically correlate the ORR activity with bulk structure and surface composition of $LaMnO_3$ nanoparticles prepared at different temperatures employing ionic liquid-based precursors. The surface chemistry of the materials was studied by low energy ion scattering (LEIS) and X-ray photoemission spectroscopy (XPS), whereas the bulk structure was investigated by transmission electron microscopy (TEM), X-ray diffraction (XRD), and X-ray absorption spectroscopy (XAS). A key aspect of our approach is the estimation of the number of surface Mn sites based on the electrochemical responses of the particles supported on mesoporous carbon electrodes. Our

[a] Dr. V. Celorrio, Prof. D. J. Fermín
School of Chemistry, University of Bristol
Cantocks Close, Bristol BS8 1TS, UK
E-mail: v.celorrio@ucl.ac.uk
David.Fermin@bristol.ac.uk
[b] Dr. L. Calvillo, Prof. G. Granozzi
Dipartimento di Scienze Chimiche and Unità di Ricerca INSTM
Università di Padova
Via Marzolo 1, 35131 Padova, Italy
[c] Dr. C. A. M. van den Bosch, Dr. A. Aguadero
Department of Materials, Imperial College London
London SW7 2AZ, U.K
[d] Prof. A. E. Russell
School of Chemistry, University of Southampton
Highfield, Southampton, U.K
[e] Dr. V. Celorrio
UK Catalysis Hub, Research Complex at Harwell, RAL, Oxford, OX11 0FA, UK
and
Kathleen Lonsdale Building, Department of Chemistry, University College London, Gordon Street, London, WC1H 0AJ, UK

Supporting information for this article is available on the WWW under https://doi.org/10.1002/celc.201800729

Special Issue *An invited contribution to a Special Issue on Single-Entity Electrochemistry*

studies show a complex non-monotonic dependence of the ORR activity with the calcination temperature. However, normalisation of the ORR activity to the number of reducible Mn sites shows that the mean activity of single Mn sites increases with temperature above 700 °C, which coincides with the appearance of the characteristic XPS signature of oxygen in the perovskite lattice.

2. Results and Discussion

2.1. $LaMnO_3$ Nanoparticle Bulk Characterization as a Function of Synthesis Temperature

Figure 1a shows the XRD patterns of the $LaMnO_3$ nanoparticles prepared at various temperatures, as well as the allowed Bragg reflections for the rhombohedral (*R3-c*) phase. All the crystal structures were indexed to this phase, although the relatively broad XRD features arising from the small crystallite sizes of calcined at 600 °C ($LaMnO_3$-600C), at 650 °C ($LaMnO_3$-650C) and at 700 °C ($LaMnO_3$-700C) may introduce a degree of uncertainty in the identification of the phase group. The crystal structures of $LaMnO_3$-800C, $LaMnO_3$-850C, $LaMnO_3$-900C and $LaMnO_3$-950C were accurately refined in the rhombohedral phase without the need for any added structural distortions and Table S1 summarizes the unit cell parameters and discrepancy factors after the refinements of the higher temperature structures. The mean size of the crystalline domains was calculated using the (200) Bragg peak ($2\theta \approx 47°$) and summarised in Table S2, showing an overall increase from 16 to 38 nm with increasing synthesis temperature. Figure 1b shows representative transmission electron micrographs of a selection of the samples (images corresponding to the remaining temperatures are shown in Figure S1a). Analysis of over 100 particles in each sample image yielded mean particle sizes in a similar range to the crystalline domains obtained from the XRD, i.e. 17.2 ± 3.5 (600 °C) to 45.4 ± 8.9 nm (950 °C). It should be noticed that $LaMnO_3$-700C shows the smallest mean particle size, suggesting a complex phase formation mechanism at this temperature. This behaviour was consistently observed in different synthesis batches. We will discuss this issue further below. Electron energy loss spectroscopy (EELS) maps in Figure S1b show the La–$M_{4,5}$, Mn–$L_{2,3}$ and O–K edges in a cluster of nanoparticles obtained for $LaMnO_3$-950 °C. A highly homogeneous elemental distribution is observed at the nanometre scale. Synthesis carried out at temperatures below 600 °C produced poorly crystalline powders (results not shown in this study).

Figure 2a contrasts the normalised Mn K-edge XANES spectra of $LaMnO_3$ nanoparticles synthesised at different temperatures. The spectral line shapes are similar for all samples, with the exception of $LaMnO_3$-700C, showing a pre-edge feature (displayed in more detail in the inset) and a main resonance at the edge, characteristic of the Mn octahedral coordination.[19] Two features can be distinguished in the pre-edge region, which has contributions from both Mn^{3+} and Mn^{4+}. Following protocols reported elsewhere,[8] a mean Mn oxidation state of approximately +3.2 can be estimated from the position of the main edge independently of the syntesis temperature.

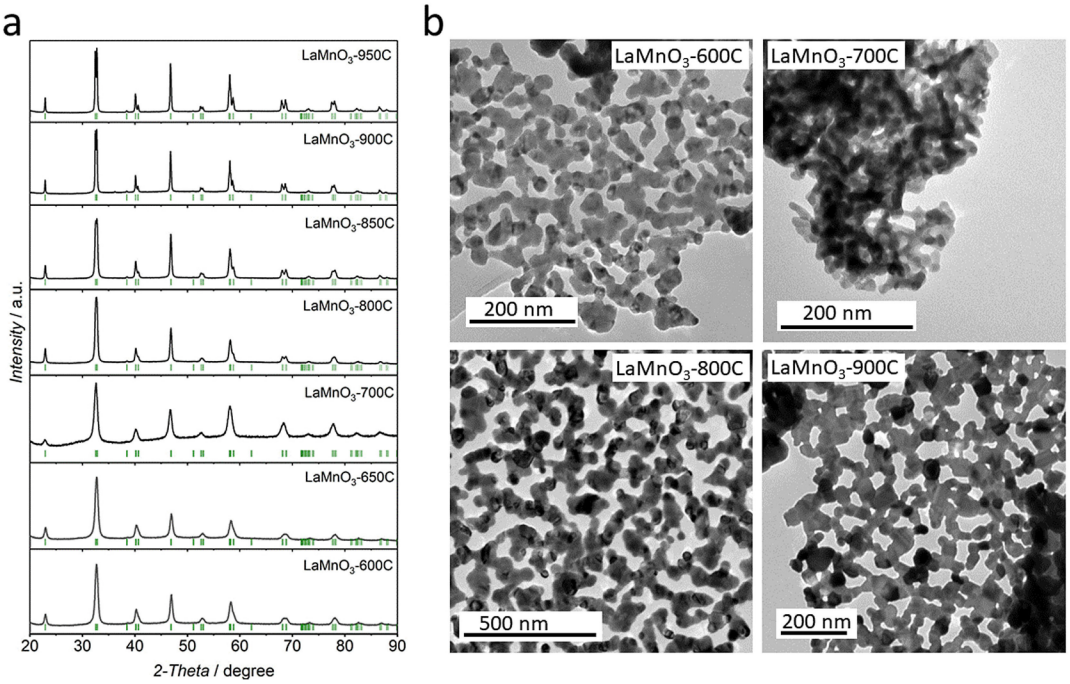

Figure 1. a) XRD patterns of $LaMnO_3$-600C, $LaMnO_3$-650C, $LaMnO_3$-700C, $LaMnO_3$-800C, $LaMnO_3$-850C, $LaMnO_3$-900C and $LaMnO_3$-950C. The green bars correspond to the positions of the allowed Bragg reflections for the rhombohedral (*R3-c*) phase. b) Characteristic TEM images of $LaMnO_3$ particles calcined at 600, 700, 800 and 900 °C. Figure S1a includes the TEM images of the 650, 850 and 950 °C powders.

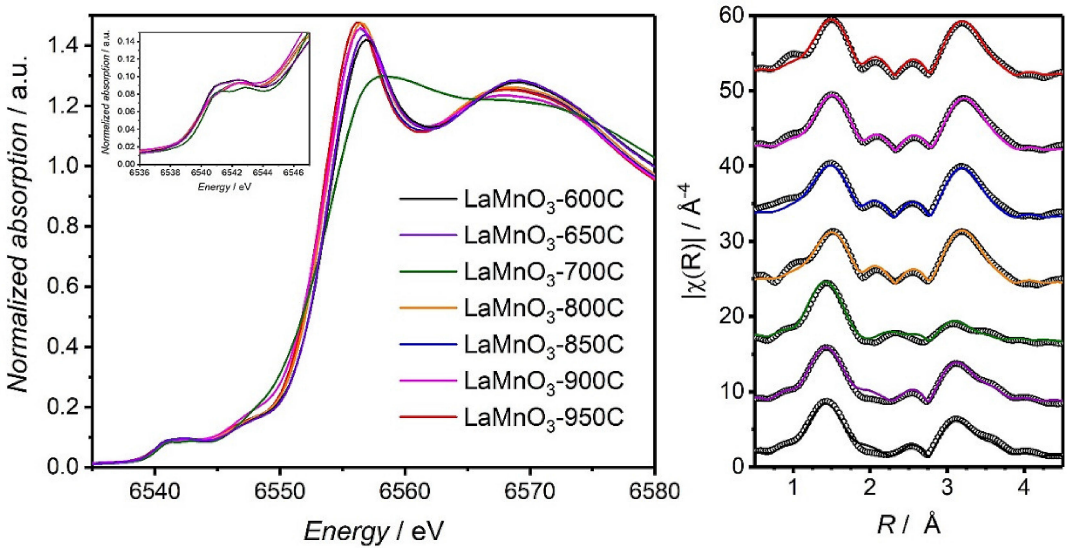

Figure 2. a) Normalised Mn K-edge XANES spectra of $LaMnO_3$ samples synthesised at different temperatures. The inset shows the Mn K pre-edge feature. b) Data (empty circles) and fits (coloured lines) of the FT signal of the k^3-weighted EXAFS.

The spectral differences illustrate small changes in local structure as a function of the synthesis temperature. Figure 2b shows the comparison between the Fourier transform (FT) of the experimental spectra (empty circles) and the best-fit simulations (coloured lines) for the whole series of synthesised materials (signals in *k*-space are shown in Figure S2). All the FTs show two strong peaks below 4 Å. The first peak at around 1.5 Å (without phase correction) corresponds to the first coordination shell (Mn–O). The second peak, above 3 Å, is associated with the second shell, which is a combination of Mn–La, Mn–Mn single scattering together with multiple scattering Mn–O paths. The starting model to fit the data was constructed using the rhombohedral unit cell of $LaMnO_3$, as deduced from the XRD Rietveld refinement, and the coordination numbers fixed to their crystallographic values. The amplitude reduction factor (S_0^2), bond lengths, Debye-Waller factors (σ^2) and the energy shift parameter (ΔE_0) were refined. The best-fit parameters are summarised in Table S3. The $LaMnO_3$ structures are composed of six oxygen atoms at equal distances, eight lanthanum atoms in a 6+2 configuration arrangement, and six manganese neighbour atoms.

The rhombohedral unit cell provided an excellent fit to both experimental spectra (Figure S2) and FTs (Figure 2b) of the particles. Fittings to an orthorhombic structure were also performed, but the fit provided unrealistically large differences in Mn–O distances introduced by Jahn-Teller distortions. It is interesting to note that phase transitions from orthorhombic to rhombohedral have been reported in the range of 700 °C.[18,20] We will demonstrate further below that changes in surface coordination of Mn are observed in the studied temperature range, which may contribute to the complexity of the XAS spectra.

2.2. Temperature Dependence of Surface Composition

Figure 3 shows low energy ion scattering (LEIS) spectra of the $LaMnO_3$-700C, $LaMnO_3$-850C and $LaMnO_3$-950C samples, revealing important differences in terms of the composition of the outermost surface of the samples. The spectrum of $LaMnO_3$-700C exhibits a well-defined Mn peak at ~2250 eV, whereas $LaMnO_3$-850C and $LaMnO_3$-950C spectra are dominated by the La signature at ~2700 eV. As recently exemplified by Symianakis et al., quantitative analysis of the spectral responses requires careful calibration of instrumental factors, surface roughness and elemental sensitivity.[18] In this study, we focus on a semi-quantitative analysis based on fitting Gaussian line shapes to the various signals and examining their relative differences over the range of samples examined (Figure S3). Integrating the La and Mn peaks yield relative La/Mn ratios of 0.67, 0.17 and 0.15

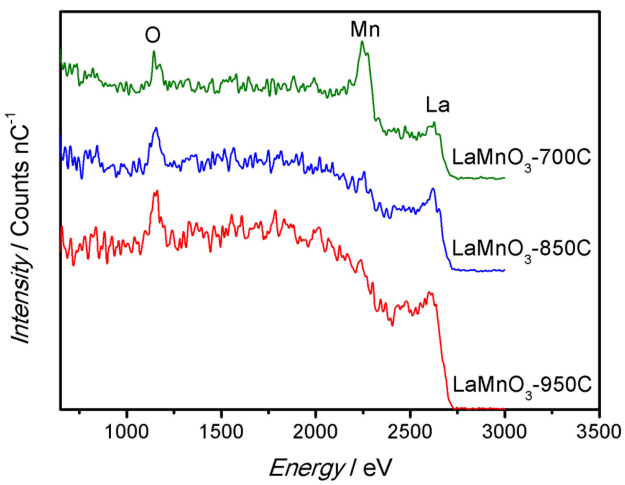

Figure 3. 3 kV He^+ LEIS spectra for $LaMnO_3$-700C, $LaMnO_3$-850C and $LaMnO_3$-950C powders.

for $LaMnO_3$-700C, $LaMnO_3$-850C and $LaMnO_3$-950C. Considering that the measurement conditions are identical in these samples, the trend suggests that the Mn content in the *first atomic layer* decreases with increasing temperature.

The effect of temperature on surface composition can be estimated in a more quantitative fashion using XPS as displayed in Figure 4. Core level photoemission spectra of O 1*s*, Mn 2*p* and La 3*d* regions for the various $LaMnO_3$ samples are shown in Figure 4, whit the C 1*s* spectra displayed in Figure S4. The O 1*s* line (Fig. 4-left panel) exhibits a maximum between 529 and 530 eV, as well as shoulder and tail extending towards higher binding energies (BEs), which can be deconvoluted into several components. The most prominent peak has contributions from both the metal-oxygen bond in the perovskite lattice (529.2 eV, peak 1)[21–22] and from La_2O_3 (529.6 eV, peak 2) associated with La surface segregation. The higher BE contributions to the O 1*s* spectra contains contributions from hydroxyl groups (531.2 eV, peak 3), carbonyl groups (532.4 eV, peak 4) and adsorbed water (533.8 eV, peak 5).[21,23–24] Analysis of the single components of the O 1*s* region can be found in Table S4. A key observation in the temperature dependence analysis is the absence of the metal-oxygen contribution (peak 1) in $LaMnO_3$-600C and $LaMnO_3$-650C, suggesting that the surface is mainly composed of binary oxides at lower synthesis temperatures.[20]

The Mn $2p_{5/2}$ line is centred at 642.2 eV for all the samples independent of the synthesis temperature (Figure 4, middle panel). The broad peak, particularly at lower temperatures, contains contributions from Mn^{3+} (641.9 eV) and Mn^{4+} (642.2 eV) signals.[21] Although an accurate determination of manganese oxidation state at the surface is challenging due to the close overlap between Mn^{3+} and Mn^{4+}, we anticipate a mixture of both oxidation states in order to compensate the positive charge deficit due to the La vacancies in the perovskite structure (linked to La segregation and formation of La_2O_3 and/or $La(OH)_3$).

The La 3*d* photoemission spectra (Figure 4, right panel) exhibits the characteristic double splitting due to the interaction between an electron from the oxygen valence band and the empty La 4*f* level. The La $3d_{5/2}$ BE is located at 834.4 eV, corresponding to La^{3+} compounds, as expected for a La-containing perovskite.[23–24] Table S5 shows that most samples exhibit surface lanthanum enrichment, most probably forming La_2O_3 which spontaneously reacts with water to form $La(OH)_3$. The dependence of A-site surface segregation on the synthesis temperature is rather complex as discussed further below.

Figure 5a shows cyclic voltammograms of the various $LaMnO_3$ nanostructures with a fixed oxide loading of 250 $\mu g_{OXIDE}\,cm^{-2}$ in argon-saturated 0.1 M KOH at 0.010 $V\,s^{-1}$. The current is normalised by the oxide real surface area (A_{oxide}), which is estimated from the specific surface area (*SSA*) shown in Table S2. All carbon supported $LaMnO_3$ nanoparticles show two cathodic reduction peaks at 0.90 V and 0.50 V, which have been previously assigned to the reduction of the Mn sites from the stoichiometric state to Mn^{2+}.[8,10,25–27] The position of the peaks remains unaltered by the synthesis temperature. The most striking difference is found in the current densities, which increase with calcination temperature in the range between 600 and 700 °C, followed by a sharp decrease with increasing temperature further. This trend cannot be rationalised in terms of the changes in the nanoparticle size on the basis that the current is already normalised by A_{oxide}. On the other hand, this behaviour suggests a non-monotonical change in the number density of surface Mn sites (Γ_{Mn}) with increasing the synthesis temperature.

The effect of synthesis temperature on the surface Mn/La ratio (as estimated from XPS) and on Γ_{Mn} are contrasted in Figures 5b and 5c, respectively. Γ_{Mn} was calculated by integrat-

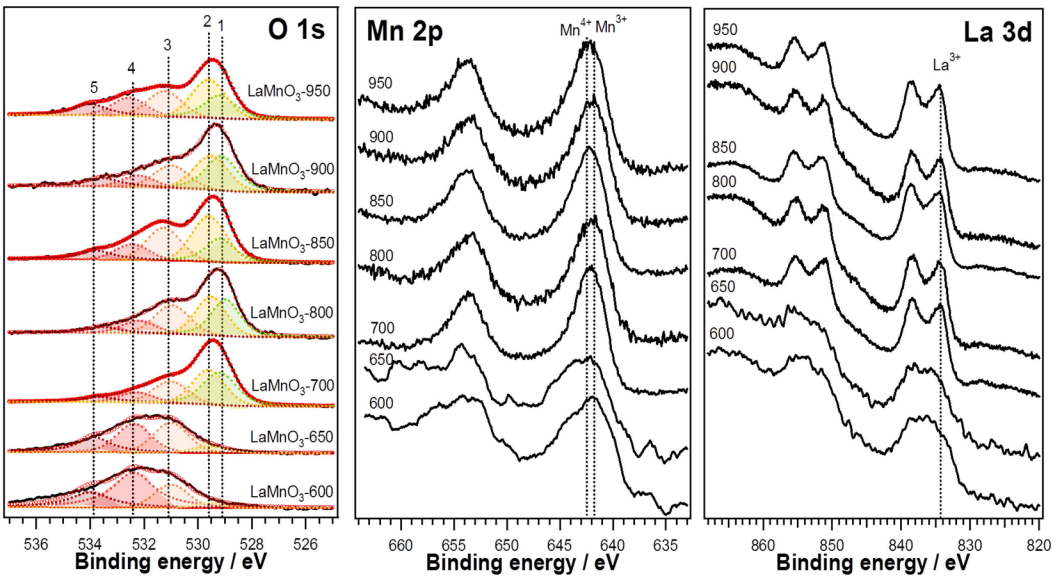

Figure 4. (left) O 1*s*, (middle) Mn 2*p* and (right) La 3*d* photoemission spectra collected in normal emission using non-monochromatised Al K_α X-ray source for samples treated at different temperatures. Assignment of components in O 1*s* region: (1) Oxygen in the perovskite lattice; (2) lanthanum oxide; (3) hydroxyl species OH^-; (4) carbonyl groups; (5) adsorbed water.

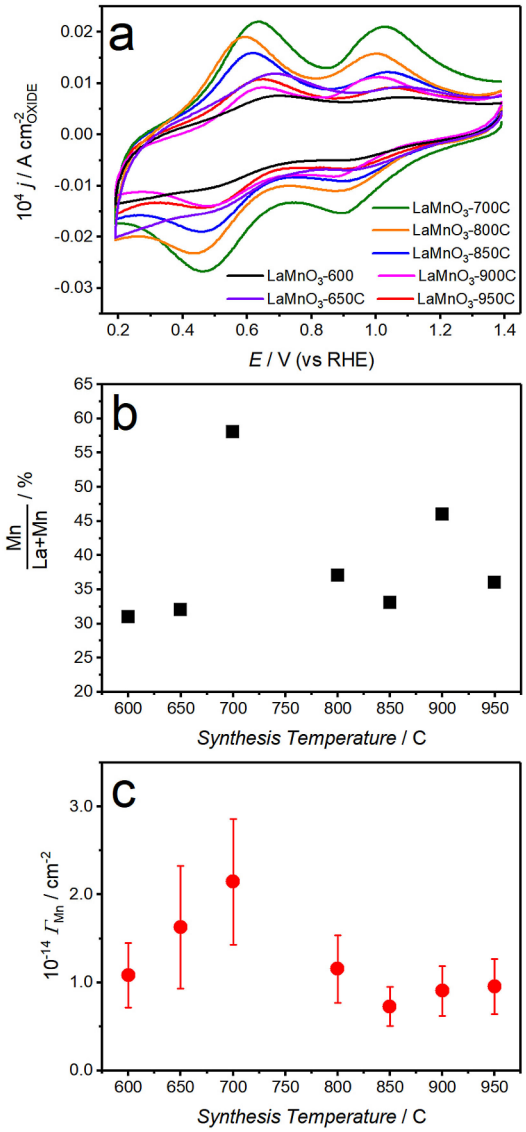

Figure 5. a) Cyclic voltammograms of the $LaMnO_3$ nanoparticles, synthesised at different temperatures, in Ar-saturated 0.1 M KOH solution at 0.010 V s^{-1}. Oxide nanoparticles were supported on a Vulcan layer with a total oxide content of 250 μg cm^{-2}. b) Mn/La ratio estimated from the XPS data in Figure 4. c) Number density of surface Mn site (Γ_{Mn}), estimated from the Faradaic charge in the voltammetric responses and considering a change of the Mn oxidation state from +3.2 to +2 across the potential range, normalised by A_{oxide}.

ing the cathodic current peaks across the potential range assuming a change of oxidation state from +3.2 to +2,[7–8,10] and normalised by A_{oxide}. We observed a remarkable correspondence between both approaches, clearly indicating that the number of Mn surface sites transitions through a maximum value at 700 °C. The semi-quantitative LEIS analysis also shows a decrease in the Mn surface coverage in the first atomic layer as the temperature increases above 700 °C, which can be considered a "transition" temperature that generates the smallest particle size as shown by the TEM images (Figure 1). We also observe that the particle size increases and the crystal structure can be quantitatively refined employing the rhombohedral (*R3-c*) phase as the temperature is increased. This analysis clearly demonstrates that the synthesis temperature affects the surface composition of the nanostructures.

2.3. Mean Electrocatalytic Activity of single surface Mn sites towards the ORR reaction

Figure 6 displays current-voltage curves at a disk containing Vulcan-supported $LaMnO_3$ nanostructures (i_{DISK}, bottom panel) and a Pt ring (i_{RING}, top panel) rotating at 1600 rpm in O_2-saturated 0.1 M KOH solution for catalysts prepared between 600 and 900 °C (for full set of data see Figure S5). $LaMnO_3$-600C exhibits the most negative ORR onset potential as well as the smallest diffusional limiting currents. $LaMnO_3$-700C, $LaMnO_3$-800C and $LaMnO_3$-900C show diffusional limiting currents typical of a 4-electron reduction (Figure S6-left panel), and peroxide yields below 20% as estimated from the ring currents (Figure S6-right panel). $LaMnO_3$-700C shows the most positive onset potential, which is consistent with our previous studies on $LaMnO_3$ oxides.[7–10,17] At temperatures above 700 °C, the ORR onset appears to slightly shift towards more negative potentials. In general, we can see that the onset potential of Mn site reduction (as seen in Figure 5a) overlaps with the ORR onset potential, reinforcing the notion that changes in the oxidation state of Mn sites triggers the 4-electron oxygen reduction pathway.[7–8,17]

Figure 7 contrasts the effect of the synthesis temperature on the kinetically limited current density at 0.65 V normalised by A_{oxide} ($j_k = i_k/A_{oxide}$) and by the number of redox active Mn sites ($i_k\ \Gamma_{Mn}^{-1}\ A_{oxide}^{-1}$), while the conventional mass normalisation is shown in Figure S7. i_k is estimated by extrapolating the Faradaic current to infinite angular rotation based on Koutecky-Levich formalism. Comparing i_k at 0.65 V can be rationalised in terms of: (1) the contribution of the electron transfer kinetic is significant in this potential and (2) there is significant contrast between the current in the presence of catalysts and the carbon support.[17] Figure 7a show that j_k goes

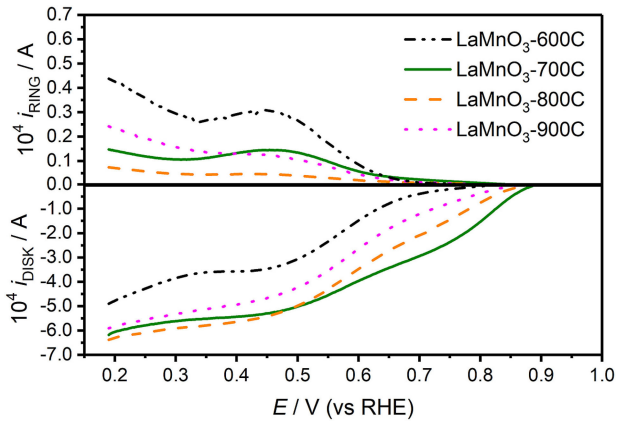

Figure 6. Rotating ring-disk electrode (RRDE) responses of the various $LaMnO_3$ nanoparticles supported at a Vulcan layer at 1600 rpm in O_2-saturated 0.1 M KOH at 0.010 V/s. The Pt ring was held at a constant potential of 1.10 V. The oxide loading in each electrode was 250 μg cm^{-2}.

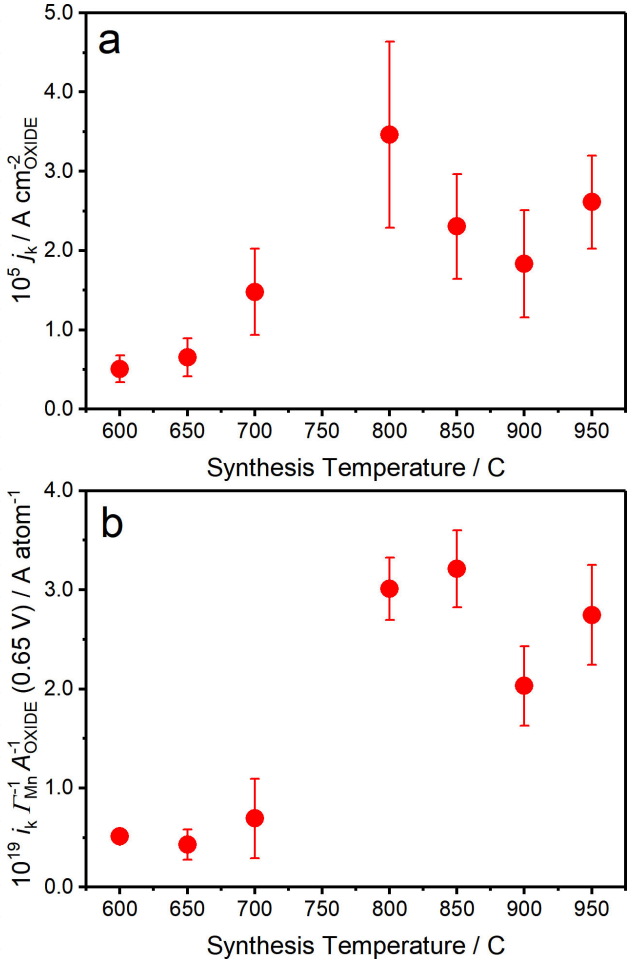

Figure 7. Kinetically limiting current at 0.65 V vs RHE normalised by: a) oxide real surface area ($j_k = i_k/A_{oxide}$) and, b) the number of redox active Mn sites ($i_k\ \Gamma_{Mn}^{-1}\ A_{oxide}^{-1}$). For comparison, conventional normalisation by the catalyst mass loading is displayed in Figure S7. The trend in b) is directly proportional to the turn-over frequency of the Mn active sites.

through at maximum value at 800 °C, while conventional normalisation by mass shows a maximum closer to 700 °C (Figure S7). These trends reflect two important phenomena, the specific surface area (SSA) and Γ_{Mn} go through a maximum at this critical temperature. Consequently, the high performance of $LaMnO_3$-700C as seen in Figure 6 has a strong contribution from the small particle size and the high number density of Mn sites, which is also consistent with the XPS (Figure 5b) and LEIS (Figure 3) data. Normalising the kinetic current by A_{oxide} reveals that particles prepare at higher temperature the activity of the catalysts is somewhat higher for particles prepare at temperatures above 700 °C.

A different trend is observed in the case of i_k normalised by the number of redox active Mn sites (Figure 7b). The parameter $i_k\ \Gamma_{Mn}^{-1}\ A_{oxide}^{-1}$ is a direct representation of the turn over frequency (TOF) of active Mn sites. As discussed above, the overlap between the onset potentials for ORR and Mn site reduction provide a clear evidence that the population of Mn sites represented by Γ_{Mn} is the key drive for the catalytic reaction. The trend shows a size increase in the TOF at temperatures above 700 °C. It is interesting to notice that oxygen coordinated in a perovskite lattice, as probed by XPS (Figure 4), becomes detectable around this transition temperature. This observation is significant as it provides clear evidence of the nature of the most active site at the surface of these complex materials. Furthermore, our analysis based on the electrochemical TOF provides a more accurate analysis of the overall reactivity of individual Mn sites, which can be used to construct fundamental structure-activity relationships. Finally, we anticipate that careful tuning of the synthesis conditions in the range of 700 to 800 °C, with a systematic variation of the temperature programme, would lead to $LaMnO_3$ particles with optimal particle size and Mn surface coordination for catalysing ORR.

3. Conclusions

A systematic structural-activity analysis of $LaMnO_3$ oxide nanoparticles towards the oxygen reduction reaction reveals that the synthesis temperature plays a crucial role in determining the mean activity of surface Mn sites. Employing an ionic liquid-based synthesis method, in the presence of cellulose, highly crystalline $LaMnO_3$ nanoparticles with a diameter in the range of 16 to 38 nm were prepared by varying the temperature between 600 and 950 °C. Although particle size increases with temperature, this trend is non-monotonical, showing a minimum in particle size at 700 °C. XPS showed that the Mn/La ratio reaches a maximum at this temperature, which also coincides with the appearance of characteristic oxygen XPS signature linked to perovskite coordination. As the temperature is increased above 700 °C, XRD and EXAFS patterns show a well-defined rhombohedral phase structure, while XPS and LEIS shows a decrease of the Mn/La ratio at the surface. Electrochemical responses associated with surface Mn sites per unit of area of oxide show a maximum value at 700 °C. The activity of the catalysts towards the ORR normalised either by mass or oxide real surface area undergoes through a maximum between 700 and 800 °C. This trend is consistent with the fact that the mean particle size goes through a minimum while the number density of redox active Mn sites (active sites) is maximum in this narrow temperature range. However, the mean activity of single Mn sites (equivalent to TOF) shows a step increase as the synthesis temperature is increased above 700 °C. The increase in activity coincides with the appearance of the XPS signature of oxygen in the perovskite lattice. We conclude that mass normalisation of the catalyst performance is useful for composition optimisation, but it may lead to erroneous structure-activity relationships. On the other hand, normalising by the number of redox active Mn sites allows decoupling non-trivial contributions such as changes in specific surface area and A-site segregation, unveiling the intrinsic activity of this complex materials.

4. Associated Content

All the data presented in this paper can be freely accessed from the Bristol's Research Data Repository (https://doi.org/10.5523/bris.3era7kdsvgvur2nclshqy7u762).

Experimental Details

Synthesis of Materials

The preparation of phase-pure $LaMnO_3$ nanoparticles is based on an ionic liquid method incorporating cellulose.[8,28–29] A 1 mL aqueous mixture of 0.1 M $La(NO_3)_3$ and 0.1 M $Mn(NO_3)_3$ was prepared from the anhydrous salts (Sigma Aldrich). This solution was mixed with 1 mL of 1-ethyl-3-methylimidazolium acetate (Sigma Aldrich) and heated at 80 °C for 3 hours to facilitate evaporation of water. Microcrystalline cellulose (100 mg, 10 wt.%) was subsequently added yielding a smooth, homogeneous gel. The dehydrated precursor gel was calcined immediately after preparation, under air, for 2 hours at different temperatures of 600 °C, 650 °C, 700 °C, 800 °C, 850 °C, 900 °C and 950 °C and a heating rate of 5 °C/min.

X-ray Diffraction and Rietveld Refinement

X-ray diffraction (XRD) patterns were recorded using a Bruker AXS D8 Advance diffractometer with a θ-θ configuration, using Cu Kα radiation ($\lambda = 0.154$ nm). Experiments were run between 10 and 90 degrees, using a step size of 0.02 degrees.

Microscopy

Transmission electron microscopy (TEM) and high-resolution TEM analysis were performed using a JEOL JEM-1400Plus and a JEOL JEM 2100, respectively. Samples for TEM were produced by placing 1 mL drops of the oxide particles dissolved in ethanol on a 3 mm diameter carbon-coated copper grid. Mean particle diameters were estimated from at least 100 nanoparticles per sample.

Low Energy Ion Scattering

LEIS data was obtained using an ION-TOF GmbH Qtac instrument under UHV conditions of at least 1.1×10^{-8} mbar. Incident ions were produced by a heated filament in He and Ne ion mixed gas atmosphere, accelerated through a potential to achieve a 3 kV He^+ ion beam. Scattered ions were detected at 145° by a double toroidal analyser. An unfocused electron shower was used to avoid charging of the surface. For the collected spectra there was a dose density of $2.39–2.92 \times 10^{14}$ ions cm^{-2} over an area of 1000 μm^2 and therefore a total dose of $2.39–2.92 \times 10^{12}$ ions.

X-ray Photoelectron Spectroscopy

Photoemission data was obtained in a custom designed UHV system equipped with an EA 125 Omicron electron analyser with five channeltrons, working at a base pressure of 10^{-10} mbar. Core level photoemission spectra (C 1*s*, O 1s, Mn 2*p* and La 3*d* regions) were collected in normal emission at room temperature with a non-monochromatised Al K_α X-ray source (1486.7 eV) and using 0.1 eV steps, 0.5 s collection time and 20 eV pass energy. The binding energies (BE) were referenced to the C 1s peak at 284.6 eV.

X-ray Absorption Measurements

EXAFS spectra were recorded on beamline B18 at Diamond Light Source operating with a ring energy of 3 GeV and at a current of 300 mA.[30] The monochromator comprises Si(111) crystals operating in Quick EXAFS mode. Calibration of the monochromator was carried using a Mn foil prior to the measurements. Pellets of the different samples were collected in transmission mode at the Mn K-edge (6539 eV), simultaneously with the Mn foil. A total of three spectra were averaged for each sample. The data were analysed using the Athena and Arthemins programs,[31] which implement the FEFF6 and IFEFFIT codes.[32] Fits were carried out using a *k* range of 3–11 $Å^{-1}$ and a *R* range of 1.0–4.0 Å with multiple *k* weightings of 1, 2 and 3. To perform the fittings, the coordination numbers were fixed to the crystallographic values; interatomic distances and Debye-Waller factors were fitted.

Electrochemistry

Electrochemical measurements were conducted in a three-electrode cell using a rotating ring-disk electrode (RRDE) fitted to an ALS rotation controller and connected to a CompactStat bipotentiostat (Ivium). The RRDE electrode consisted of a 4 mm glassy carbon disk surrounded by a Pt ring. The collection efficiency was experimentally determined to be 0.4. Hg/HgO (in 1 M NaOH, IJ Cambria) was used as the reference electrode. The potentials in this work are referenced to the reversible hydrogen electrode (RHE) scale. Measurements were carried out in 0.1 M KOH saturated electrolyte with either purified Ar or O_2 (BOC). A thin-film catalyst layer was deposited on the glassy carbon electrode using a two-step drop-casting method with two different inks. An ink containing Vulcan XC-72 carbon and Na^+-exchanged Nafion® (5 wt%, Sigma-Aldrich) was deposited on the glassy carbon disk, followed by deposition of an aqueous suspension of the oxide. The final loading in the catalyst layer for each electrode was controlled at 250 $\mu g_{OXIDE}\,cm^{-2}$, 50 $\mu g_{VULCAN}\,cm^{-2}$ and 50 $\mu g_{NAFION}\,cm^{-2}$ (per geometric surface area of the electrode).

Acknowledgements

V.C. gratefully acknowledges the UK National Academy and the Royal Society by the support though the Newton International Fellows program. V.C., A.R., A.A. and D.J.F. kindly thank the UK Catalysis Hub for resources and support provided via the membership of the UK Catalysis Hub Consortium and funded by EPSRC (EPSRC grants EP/K014706/1 and EP/K014714/1). TEM studies were carried out at the University of Bristol Chemistry Imaging Facility with equipment funded by UoB and EPSRC (EP/K035746/1 and EP/M028216/1). The authors wish to acknowledge the Diamond Light Source for provision of beamtime (SP10306 and SP15151). The authors also acknowledge Mr. Neil Wilkinson (Gatan UK) and Mr. Jonathan A. Jones (former Chemical Imaging Facility, University of Bristol) for the assistance with EELS imaging.

Conflict of Interest

The authors declare no conflict of interest.

Keywords: electrocatalysis · kinetics · $LaMnO_3$ · nanoparticles · oxygen reduction reaction

[1] J. Stacy, Y. N. Regmi, B. Leonard, M. Fan, *Renewable Sustainable Energy Rev.* **2017**, *69*, 401–414.
[2] V. R. Stamenkovic, D. Strmcnik, P. P. Lopes, N. M. Markovic, *Nat. Mater.* **2016**, *16*, 57.
[3] J. Hwang, R. R. Rao, L. Giordano, Y. Katayama, Y. Yu, Y. Shao-Horn, *Science* **2017**, *358*, 751–756.
[4] M. Risch, *Catalysts* **2017**, *7*, 154.
[5] M. P. Browne, C. Domínguez, P. E. Colavita, *Curr. Opin. Electrochem.* **2017**.
[6] K. A. Stoerzinger, M. Risch, B. Han, Y. Shao-Horn, *ACS Catal.* **2015**, *5*, 6021–6031.
[7] V. Celorrio, E. Dann, L. Calvillo, D. J. Morgan, S. R. Hall, D. J. Fermin, *ChemElectroChem* **2016**, *3*, 283–291.
[8] V. Celorrio, L. Calvillo, E. Dann, G. Granozzi, A. Aguadero, D. Kramer, A. E. Russell, D. J. Fermin, *Catal. Sci. Technol.* **2016**, *6*, 7231–7238.
[9] V. Celorrio, L. Calvillo, G. Granozzi, A. E. Russell, D. J. Fermin, *Top. Catal.* **2018**, *61*, 154–161.
[10] V. Celorrio, L. J. Morris, M. Cattelan, N. A. Fox, D. J. Fermin, *MRS Commun.* **2017**, *7*, 193–198.
[11] J. Suntivich, H. A. Gasteiger, N. Yabuuchi, H. Nakanishi, J. B. Goodenough, Y. Shao-Horn, *Nat. Chem.* **2011**, *3*, 647–651.
[12] Y. Wang, H.-P. Cheng, *J. Phys. Chem. C* **2013**, *117*, 2106–2112.
[13] G. Pilania, R. Ramprasad, *Surf. Sci.* **2010**, *604*, 1889–1893.
[14] E. A. Kotomin, Y. A. Mastrikov, E. Heifets, J. Maier, *Phys. Chem. Chem. Phys.* **2008**, *10*, 4644–4649.
[15] E. A. Ahmad, G. Mallia, D. Kramer, A. R. Kucernak, N. M. Harrison, *J. Mater. Chem. A* **2013**, *1*, 11152–11162.
[16] Y. Zhou, S. Xi, J. Wang, S. Sun, C. Wei, Z. Feng, Y. Du, Z. J. Xu, *ACS Catal.* **2018**, *8*, 673–677.
[17] G. Gobaille-Shaw, V. Celorrio, L. Calvillo, L. J. Morris, G. Granozzi, D. J. Fermín, *ChemElectroChem* **2018**, *doi:10.1002/celc.201800052*.
[18] E. Symianakis, D. Malko, E. Ahmad, A.-S. Mamede, J.-F. Paul, N. Harrison, A. Kucernak, *J. Phys. Chem. C* **2015**, *119*, 12209–12217.
[19] J. García, M. C. Sánchez, G. Subías, J. Blasco, *J. Phys. Condens. Matter* **2001**, *13*, 3229.
[20] F. Licci, G. Turilli, P. Ferro, A. Ciccarone, *J. Am. Ceram. Soc.* **2003**, *86*, 413–419.
[21] C. N. Borca, S. Canulescu, F. Loviat, T. Lippert, D. Grolimund, M. Döbeli, J. Wambach, A. Wokaun, *Appl. Surf. Sci.* **2007**, *254*, 1352–1355.
[22] N. Nuns, A. Beaurain, M. T. N. Dinh, A. Vandenbroucke, N. De Geyter, R. Morent, C. Leys, J. M. Giraudon, J. F. Lamonier, *Appl. Surf. Sci.* **2014**, *320*, 154–160.
[23] R. Dudric, A. Vladescu, V. Rednic, M. Neumann, I. G. Deac, R. Tetean, *J. Mol. Struct.* **2014**, *1073*, 66–70.
[24] N. A. Merino, B. P. Barbero, P. Eloy, L. E. Cadús, *Appl. Surf. Sci.* **2006**, *253*, 1489–1493.
[25] M. Risch, K. A. Stoerzinger, B. Han, T. Z. Regier, D. Peak, S. Y. Sayed, C. Wei, Z. Xu, Y. Shao-Horn, *J. Phys. Chem. C* **2017**, *121*, 17682–17692.
[26] F. H. B. Lima, M. L. Calegaro, E. A. Ticianelli, *Electrochim. Acta* **2007**, *52*, 3732–3738.
[27] Y. Gorlin, B. Lassalle-Kaiser, J. D. Benck, S. Gul, S. M. Webb, V. K. Yachandra, J. Yano, T. F. Jaramillo, *J. Am. Chem. Soc.* **2013**, *135*, 8525–8534.
[28] V. Celorrio, D. Tiwari, D. J. Fermin, *J. Phys. Chem. C* **2016**, *120*, 22291–22297.
[29] M. I. Díez-García, V. Celorrio, L. Calvillo, D. Tiwari, R. Gómez, D. J. Fermín, *Electrochim. Acta* **2017**, *246*, 365–371.
[30] A. J. Dent, G. Cibin, S. Ramos, A. D. Smith, S. M. Scott, L. Varandas, M. R. Pearson, N. A. Krumpa, C. P. Jones, P. E. Robbins, *J. Phys. Conf. Ser.* **2009**, *190*, 012039.
[31] B. Ravel, M. Newville, *J. Synchrotron Radiat.* **2005**, *12*, 537–541.
[32] M. Newville, *J. Synchrotron Radiat.* **2001**, *8*, 96–100.

Manuscript received: May 31, 2018
Accepted Article published: June 22, 2018
Version of record online: July 10, 2018